Dynamic traction of lattice-confined platinum atoms into mesoporous carbon matrix for hydrogen evolution reaction

Lou, David Xiong Wen; Zhang, Huabin; An, Pengfei; Zhou, Wei; Guan, Bu Yuan; Zhang, Peng; Dong, Juncai

2018

Zhang, H., An, P., Zhou, W., Guan, B. Y., Zhang, P., Dong, J., et al. (. (2018). Dynamic traction of lattice-confined platinum atoms into mesoporous carbon matrix for hydrogen evolution reaction. Science Advances, 4(1), eaao6657-.

https://hdl.handle.net/10356/85419

https://doi.org/10.1126/sciadv.aao6657

CHEMISTRY

Dynamic traction of lattice-confined platinum atoms into mesoporous carbon matrix for hydrogen evolution reaction

Huabin Zhang,[1] Pengfei An,[2] Wei Zhou,[3] Bu Yuan Guan,[1] Peng Zhang,[1] Juncai Dong,[2] Xiong Wen (David) Lou[1]*

Constructing atomically dispersed platinum (Pt) electrocatalysts is essential to build high-performance and cost-effective electrochemical water-splitting systems. We present a novel strategy to realize the traction and stabilization of isolated Pt atoms in the nitrogen-containing porous carbon matrix (Pt@PCM). In comparison with the commercial Pt/C catalyst (20 weight %), the as-prepared Pt@PCM catalyst exhibits significantly boosted mass activity (up to 25 times) for hydrogen evolution reaction. Results of extended x-ray absorption fine structure investigation and density functional theory calculation suggest that the active sites are associated with the lattice-confined Pt centers and the activated carbon (C)/nitrogen (N) atoms at the adjacency of the isolated Pt centers. This strategy may provide insights into constructing highly efficient single-atom catalysts for different energy-related applications.

INTRODUCTION

Hydrogen fuel is one of the most promising clean and sustainable energy sources for modern society in view of the forthcoming fossil fuel exhaustion and environmental issues (*1*, *2*). As an attractive approach to produce hydrogen fuel, electrochemical water splitting driven by highly efficient electrocatalysts has been investigated intensively (*3*). Up to now, Pt and Pt-based alloys are demonstrated to be the most effective electrocatalysts for hydrogen evolution reaction (HER) (*4*). However, the high cost and low abundance of Pt severely limit the large-scale application of Pt-based electrocatalysts. This problem can be addressed by improving the utilization efficiency of Pt atoms. Because only the atoms at the surface or subsurface of electrocatalysts are involved in the catalytic process, reducing the size of Pt-based electrocatalysts to clusters or even to single atoms is one of the most promising approaches to improve the utilization efficiency of Pt atoms (*5*–*7*). Moreover, the isolated Pt centers, having low coordination and unsaturated configuration, are expected to be more active than conventional nanosized Pt particles (*8*–*10*). Nevertheless, the extremely high surface energy makes isolated metal atoms unstable during the electrocatalytic reactions (*11*–*14*). Thus, confining isolated Pt atoms into the crystal lattice of a host matrix is an effective strategy to prevent the aggregation of active species. Simultaneously, the direct bonding between isolated Pt centers and the host matrix may lead to promoted electrocatalytic activities and kinetics (*15*, *16*).

A porous carbon matrix (PCM) with high conductivity, good stability, and confined microenvironment is considered as an ideal support to stabilize isolated Pt centers for electrocatalysis (*17*, *18*). However, Pt single atoms loaded by the traditional wet-chemistry approach are hardly confined into the PCM. This is caused by the charge-balancing double layer generated from cationic or anionic precursors, which prevents the diffusion of Pt component into the interior of the porous matrix (*5*). Therefore, developing a facile and versatile strategy to decorate Pt single atoms into the matrix of PCM is essential for the synthesis of a highly active and stable electrocatalyst toward HER.

Herein, we report a novel dynamic reaction approach for traction and stabilization of isolated Pt atoms in the mesoporous carbon matrix through the relocation of the single-atom Pt species from the surface of the parent carbon sphere into the interior of the carbon matrix. Mesostructured polydopamine (PDA) particles, integrated with the Pt component, are innovatively used as the precursor for the synthesis of Pt single atom–decorated PCM (Pt@PCM) electrocatalyst. Pyrolysis of the precursor generates mesopores, owing to the decomposition of the surfactants in the PDA particles (*17*). Meanwhile, the internal dynamic force, as a consequence of the mesopore formation and high-temperature pyrolysis, progressively fuses Pt ions into the crystal lattice of PCM, generating the Pt@PCM electrocatalyst with high dispersity of active centers. The extended x-ray absorption fine structure (EXAFS) spectroscopy confirms that isolated Pt atoms are coordinated with surrounding C/N atoms in lattice-confined geometry. On the basis of the experimental and density functional theory (DFT) calculation results, we propose that the isolated Pt centers can activate the adjacent C/N atoms, making these nonmetal atoms electrocatalytically active for HER. These important findings may open new avenues toward the design of highly efficient catalysts for different energy-related applications.

RESULTS

Synthesis of the Pt@PCM electrocatalyst

The synthetic procedure of Pt@PCM is shown in Fig. 1. First, assembly of polymerized dopamine with polystyrene-*block*-poly(ethylene oxide) (PS-*b*-PEO) is performed to synthesize a PDA nanocomposite (denoted as PDA/PS-*b*-PEO). Field-emission scanning electron microscopy (FESEM) images exhibit that the obtained sample has a spherical morphology (fig. S1). Subsequently, the as-prepared PDA/PS-*b*-PEO is mixed with H_2PtCl_6 solution under decompression conditions at 50°C for 4 hours to load the Pt component on the surface of PDA/PS-*b*-PEO. Because PDA/PS-*b*-PEO with a zeta potential of −34.48 mV and platinum species (in the form of $PtCl_x^{y+}$) have opposite interfacial charges,

[1]School of Chemical and Biomedical Engineering, Nanyang Technological University, 62 Nanyang Drive, Singapore 637459, Singapore. [2]Beijing Synchrotron Radiation Facility, Institute of High Energy Physics, Chinese Academy of Sciences, Beijing 100049, China. [3]Department of Applied Physics, Tianjin Key Laboratory of Low Dimensional Materials Physics and Preparing Technology, Faculty of Science, Tianjin University, Tianjin 300072, P. R. China.
*Corresponding author. Email: xwlou@ntu.edu.sg

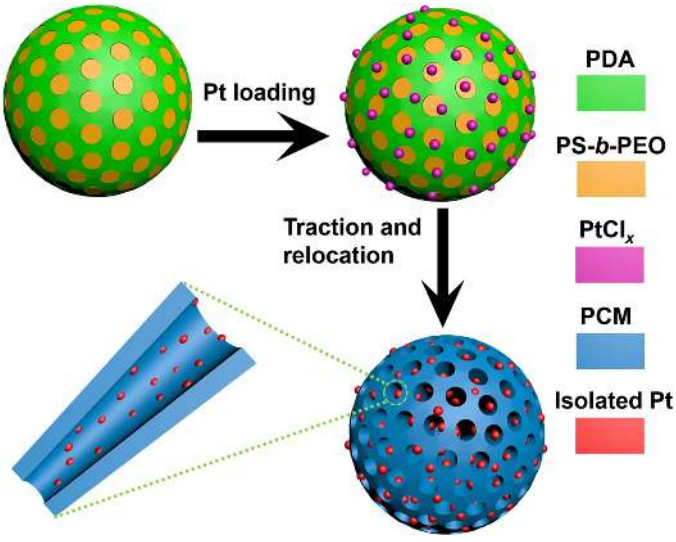

Fig. 1. Schematic illustration of the synthetic procedure of Pt@PCM. First step: loading of the Pt component onto the surface of PDA/PS-*b*-PEO to form Pt@PDA/PS-*b*-PEO. Second step: fabrication of Pt@PCM through pyrolysis of Pt@PDA/PS-*b*-PEO.

they would be assembled spontaneously through the electrostatic interaction in the solution, forming Pt-loaded PDA/PS-*b*-PEO (Pt@PDA/PS-*b*-PEO) (table S1). The Pt@PDA/PS-*b*-PEO preserves the spherical morphology, as indicated by FESEM observation (Fig. 2A and fig. S2, A and B). Transmission electron microscopy (TEM) characterization demonstrates that the as-prepared Pt@PDA/PS-*b*-PEO particles are solid without pores in the bulk (fig. S2, C to E). The as-prepared Pt@PDA/PS-*b*-PEO is converted into Pt@PCM through a stepwise pyrolysis. The carbonization process of Pt@PDA/PS-*b*-PEO is investigated by thermogravimetric (TG) analysis and differential scanning calorimetry (DSC). An obvious exothermic process accompanied by a quick weight loss starts at ~200°C and ends at ~420°C (fig. S3). This process corresponds to the removal of PS-*b*-PEO micelles, which act as the sacrificial pore-forming agent, and the transformation of PDA into the carbon matrix. As revealed by x-ray photoelectron spectroscopy (XPS) investigation, the N species in Pt@PDA/PS-*b*-PEO gradually transform from pyrrolic N to pyridinic and graphitic N in the pyrolysis process (fig. S4 and table S2). On the other hand, the Pt component is gradually fused into the carbon matrix with the increase of the pyrolysis temperature, as evidenced by the disappearance of Pt^{4+} signal and the emergence of Pt-C/N bonding in the XPS spectra (fig. S5). After pyrolysis at 800°C for 2 hours, the Pt 4f spectrum of Pt@PCM can be completely deconvoluted into Pt-C/N bonding, which demonstrates the successful confinement of Pt into the lattice of the carbon matrix.

FESEM observation shows that mesopores with a size of about 14 nm appear on the surface of Pt@PCM (Fig. 2B), which is further confirmed by high-angle annular dark-field scanning transmission electron microscopy (HAADF-STEM) characterization (Fig. 2C). These mesopores are distributed throughout the whole matrix, as indicated by the TEM image (Fig. 2D). High-resolution TEM (HRTEM) observations show that no obvious nanoparticles or clusters are found in Pt@PCM, indicating that most of the metal should remain in the form of isolated atoms (Fig. 2, E to G). The HAADF-STEM and elemental mapping images of C, N, and Pt indicate that the Pt single atoms are distributed uniformly over the entire architecture (Fig. 2, H and I). The loading amount of Pt is 0.53 weight % (wt %), as measured by inductively coupled plasma mass spectrometry (ICP-MS). The x-ray diffraction (XRD) pattern of the as-prepared samples show that only typical diffraction peaks for (002) and (101) planes of graphitic carbon have been detected, confirming the successful formation of PCM in graphitic nature and the well-dispersed feature of these platinum sites (fig. S6).

To further demonstrate the formation of Pt single atoms, we conducted EXAFS and x-ray absorption near-edge structure (XANES) analyses, which can provide more information about their chemical states and coordination structures. As shown in Fig. 3A, Pt@PCM exhibits similar Pt L_3-edge EXAFS magnitude to that of Pt@PDA/PS-*b*-PEO but produces increased intensity at the first peak of about ~1.85 Å and a slight shift to lower *R* direction. To investigate the coordination conditions of Pt centers, we performed wavelet transform (WT) analysis, which can provide a radial distance resolution and the resolution in the *K* space. A WT intensity maximum near 5.5 $Å^{-1}$ arising from the light atom coordinator is well resolved at 1.0 to 3.0 Å for Pt@PCM, whereas an intensity maximum at ~8.5 $Å^{-1}$ associated with the Pt-Pt coordination is not detected (Fig. 3E). This result confirms the successful loading of isolated Pt atoms in the carbon matrix (*19*, *20*). Further quantitative EXAFS curve fitting analysis reveals that the coordination numbers of the Pt-N/O bonding in the first coordination sphere are estimated to be 4.4 at the distance of 2.12 Å, suggesting a square-pyramidal configuration for the Pt-N/O bonding. In addition, two more distant coordination spheres corresponding to C atoms are demonstrated, which show coordination numbers of 7.8 and 8.5 at 2.75 and 3.13 Å, respectively (Fig. 3, B and C, fig. S7, and table S3). This result implies the lattice plane–confined configuration for the isolated Pt centers. The Pt L_3-edge XANES profile of Pt@PCM is also similar to that of the Pt@PDA/PS-*b*-PEO (Fig. 3D) (*8*). However, the white line intensity of Pt@PCM, which manifests the electronic density of unoccupied Pt d states, is much higher than that of Pt@PDA/PS-*b*-PEO, indicating d electron transfer from Pt to PCM. A prominent pre-edge peak at 11,550.8 eV is detected only for Pt@PCM, which is ascribed to the enhanced hybridization between the 4f and 5d orbitals in the Pt relocation process. Therefore, the EXAFS results confirm the lattice confinement of Pt atoms and demonstrate a strong coupling between isolated Pt atoms and PCM, which may greatly modify the work function of the Pt@PCM electrocatalyst (*21*).

The configuration of Pt@PCM is further confirmed by XPS investigation. The N 1s spectra of PCM demonstrate the existence of graphitic, pyridinic, and pyrrolic nitrogen species with the banding energies of 401.6, 400.6, and 398.6 eV, respectively (Fig. 4A). The existence of pyridinic N can serve as anchor points for platinum atoms (*22*). With the decoration of Pt atoms, the average binding energy of N 1s increases. Simultaneously, the ratio of pyridinic N also slightly increases (table S4). These results demonstrate the mutual interactions between the isolated Pt atoms and the carbon matrix, as well as the electron transfer between isolated Pt centers and coordinated N atoms (*23*, *24*). In addition, two peaks with binding energies of 71.28 and 74.53 eV are observed in the Pt 4f XPS spectrum of Pt@PCM, indicating the formation of Pt-C/N coordination bonds (Fig. 4B). The absence of Pt-Pt bonds at 70.89 and 74.23 eV confirms that no Pt particle is formed (*25*). Raman spectroscopy has been used to characterize the graphitization degree of carbon phases (Fig. 4C). The intensity ratio of D band to G band (I_D/I_G) increases from 0.979 to 1.069 after the Pt loading. The increase of structural disorder in graphene is associated with the decoration of isolated Pt atoms. Textural information on the nanoarchitectures is evaluated by the N_2-sorption isotherms. With the removal of PS-*b*-PEO micelles,

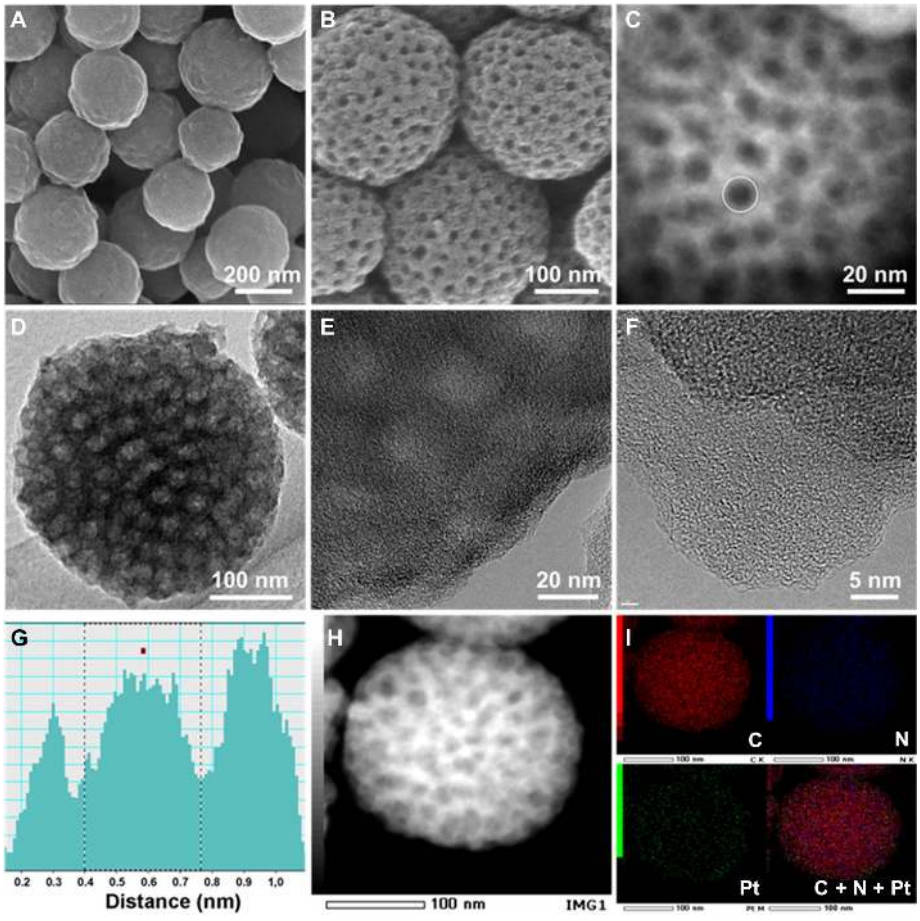

Fig. 2. Morphological, structural, and compositional characterizations of Pt@PDA/PS-*b*-PEO and Pt@PCM. (**A** and **B**) SEM images of Pt@PDA/PS-*b*-PEO (A) and Pt@PCM (B). (**C** to **I**) HAADF-STEM image (C), TEM image (D), HRTEM images (E and F), intensity profiles (G), HAADF-STEM image of the particle for mapping (H), and element mapping images of C, N, and Pt with their overlapping image (I) of Pt@PCM.

high surface areas have been obtained with a typical type IV isotherm for PCM, confirming the formation of mesopores with a uniform size of about 15 nm throughout the carbon matrix (Fig. 4D, fig. S9, and table S4) (*18*, *26*). With the implantation of the isolated Pt atoms into the carbon matrix, no obvious change has been observed. The high porosity of the PCM guarantees sufficient space for confined Pt sites to react with adsorbed water molecules, affording facile catalytic kinetics and excellent high durability. The periodicity of the pores in the Pt@PCM is also confirmed by low-angle XRD characterization (fig. S10). The single broad peak located at ~0.36° in the low-angle XRD pattern indicates that the closely packed pores in the Pt@PCM have a uniform size (*27*).

Electrochemical performance

The electrocatalytic performance of Pt@PCM for HER is examined by a typical three-electrode setup in 0.5 M H_2SO_4. The commercial Pt/C with a Pt loading of 20 wt % (Pt/C-20%) (fig. S11) and the pure PCM have also been investigated as references. As shown in the linear sweep voltammetry (LSV) curves (Fig. 5A), the PCM shows poor HER activity. However, great enhancement of activity has been observed for Pt@PCM, the onset potential of which is about 0 V versus the reversible hydrogen electrode (RHE), close to the thermodynamic potential of HER (that is, 0 V versus RHE). The onset potential of Pt@PCM is comparable with that of Pt/C-20%. The Pt@PCM requires small overpotentials of 105 and 142 mV to achieve current densities of 10 and 20 mA cm^{-2}, respectively. The required overpotentials are relatively larger than those of Pt/C-20% but much lower than those of PCM. The HER polarization curve of the catalysts with a reduced Pt loading amount of 0.095% (Pt@PCM-0.095%) presents negative-shifted onset potential. All these results compare favorably with the values reported for most HER catalysts under similar conditions and demonstrate that the decoration of Pt active sites contributes significantly to the HER activity (table S5). The electrochemically active surface area (ECSA), which is generally proportional to the double-layer capacitance (C_{dl}) of the electrocatalyst, has also been investigated. The C_{dl} is calculated from the cyclic voltammetry (CV) measurements. The results show that the C_{dl} of Pt@PCM is 0.051 F cm^{-2}, which is substantially larger than that of PCM (Fig. 5, B and C, and fig. S12) (*28*). This observation provides direct evidence for the enlarged ECSA with the decoration of Pt atoms into the matrix. The enlarged ECSA provides more active sites for enhanced HER activity.

The turnover frequencies (TOFs) based on the platinum component are calculated from the current densities obtained from the LSV curves. The TOFs exhibit a nearly linear increase with overpotential (Fig. 5D). As shown in Fig. 5E, at an overpotential of 500 mV, Pt@PCM and Pt@PCM-0.095% electrocatalysts exhibit extremely high TOFs of 43.6 and 65.5 s^{-1}, respectively. These values are about 16.6

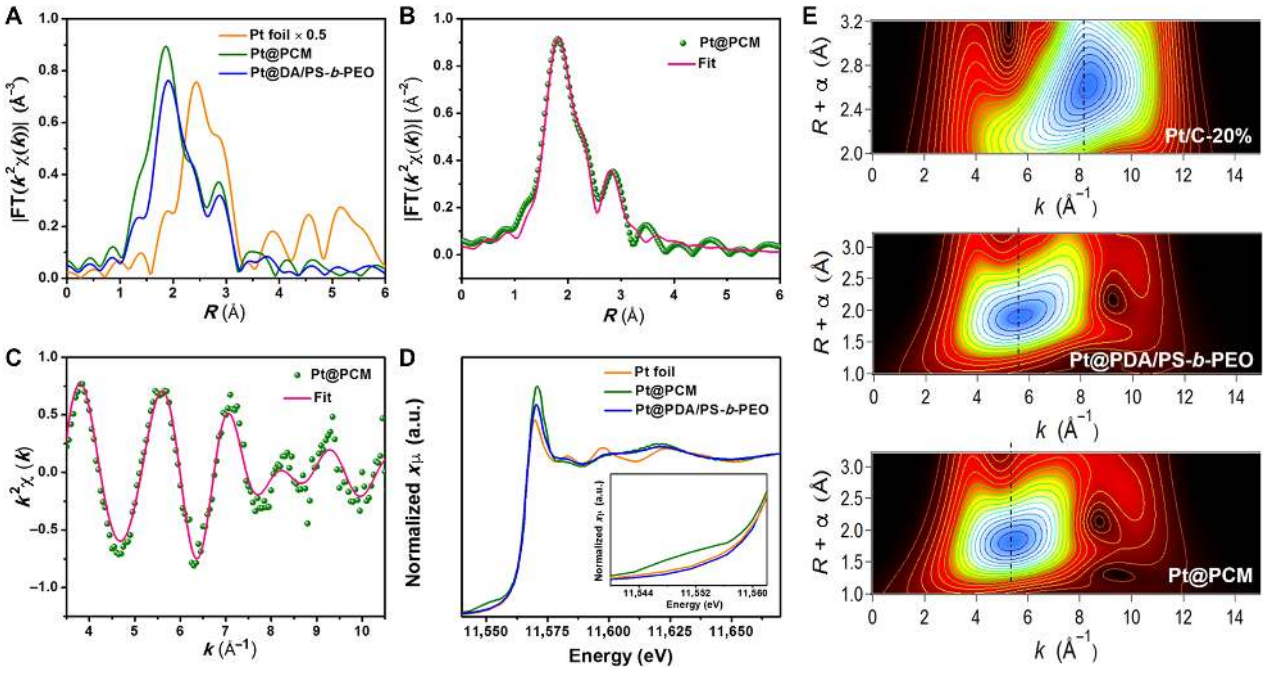

Fig. 3. EXAFS and XANES characterization results of Pt@PDA/PS-*b*-PEO and Pt@PCM. (**A**) Fourier transform (FT) magnitudes of the experimental Pt K-edge EXAFS spectra (note that the intensity of the Pt foil spectrum is reduced to half for easy comparison). (**B** and **C**) Fourier-transformed magnitudes of Pt L_3-edge EXAFS spectra in *K* space (B) and *R* space (C) for Pt@PCM. (**D**) Pt K-edge XANES experimental spectra with enlarged profile as the inset. a.u., arbitrary units. (**E**) WT for the k^3-weighted EXAFS signal.

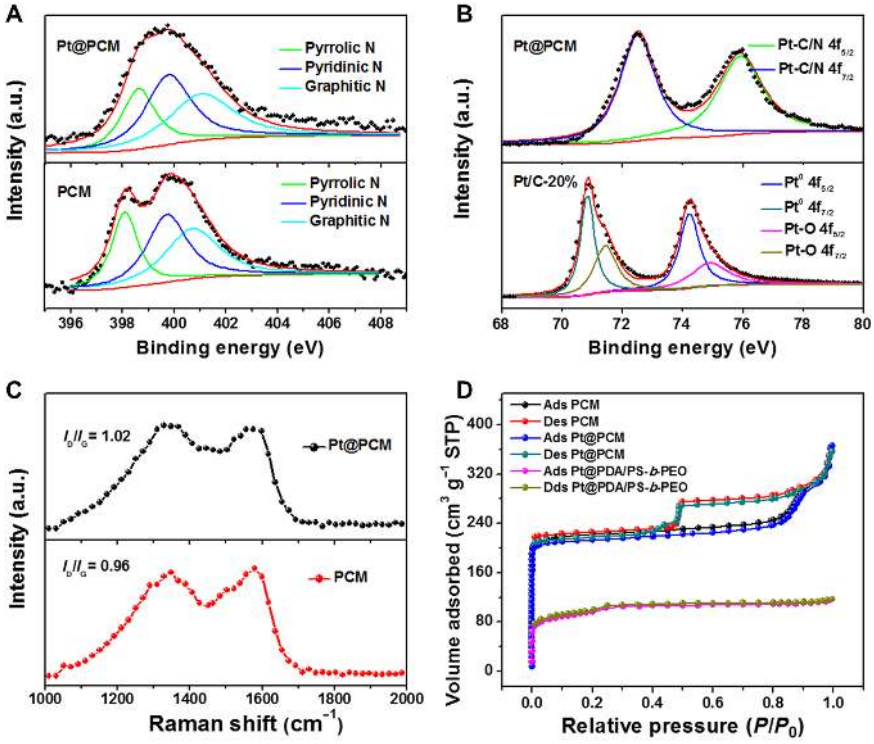

Fig. 4. Structural and compositional characterizations. (**A**) N 1s XPS spectra of PCM and Pt@PCM. (**B**) Pt 4f XPS spectra of Pt@PCM and Pt/C-20%. (**C**) Raman spectra of Pt@PCM and PCM. (**D**) N_2 sorption isotherms of PCM, Pt@PCM, and Pt@PDA/PS-*b*-PEO. Ads, adsorption; Des, desorption; STP, standard temperature and pressure.

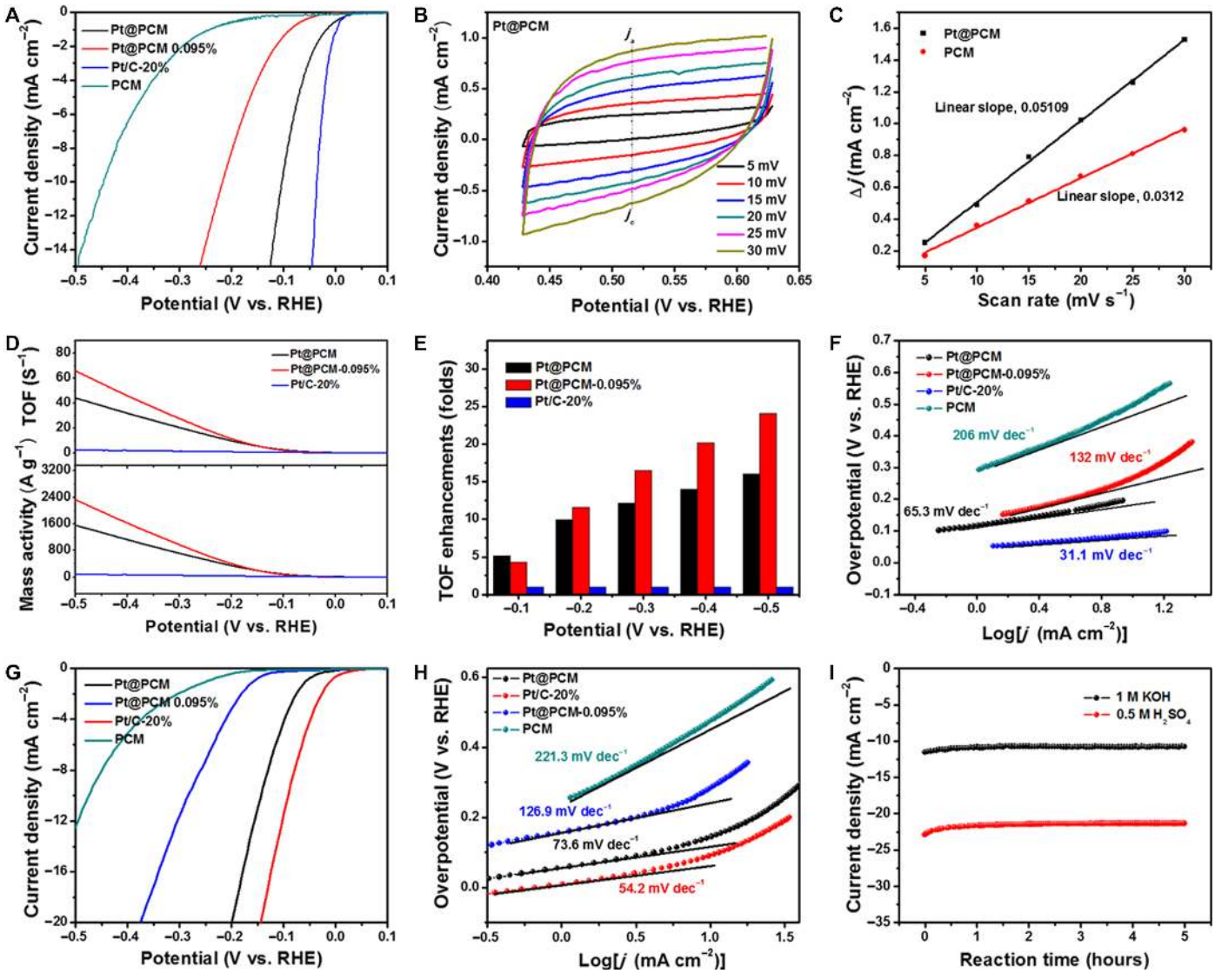

Fig. 5. Electrochemical performance characterizations. (**A**) LSV curves of various catalysts in 0.5 M H_2SO_4. (**B**) CV curves at different scan rates for the Pt@PCM. (**C**) Capacitive $\Delta j = j_a - j_c$ as a function of the scan rate of Pt@PCM and PCM catalysts. (**D**) TOFs (top) and mass activities (bottom) of catalysts at varied overpotentials. (**E**) Comparison of TOFs among catalysts at different overpotentials. (**F**) Corresponding Tafel plots for different catalysts in 0.5 M H_2SO_4. (**G**) LSV curves of various catalysts in 1.0 M KOH. (**H**) Corresponding Tafel plots for different catalysts in 1.0 M KOH. (**I**) *I-t* curves of Pt@PCM in 1 M KOH and 0.5 M H_2SO_4 media at a bias of 0.15 V versus RHE.

and 24.9 times larger than that of Pt/C-20% at identical overpotentials. Compared with other benchmarked electrocatalysts, the TOF of the Pt@PCM-0.095% sample is 15.6, 109, and 131 times higher than that of Ru/C_3N_4/C catalyst (4.2 s^{-1}) (*14*, *29*), Ni_5P_4 catalyst (0.6 s^{-1}) (*30*), and Ni-Mo catalyst (0.5 s^{-1}) (*31*) respectively under similar conditions. The mass activities are also investigated, which show almost the same trend as TOF variation. These results verify the preponderance of isolated Pt atom confinement when compared with commercial Pt/C.

To investigate the mechanistic insights into the outstanding catalytic activity of Pt@PCM for HER, we evaluated catalytic kinetics from the Tafel plots (Fig. 5F). Pt@PCM shows a Tafel slope of 63.7 mV dec^{-1}, whereas Pt@PCM-0.095% and PCM exhibit Tafel slopes of 132 and 206 mV dec^{-1}, respectively. The Tafel slope reflects the rate-determining step (RDS) of a catalytic process (*28*, *29*). The RDS for PCM and Pt@PCM-0.095% is the Volmer step, whereas the RDS for Pt@PCM is the Heyrovsky step, so that the Volmer-Heyrovsky mechanism can be confirmed. This result also suggests that the loading amount of isolated Pt sites can directly influence the RDS in the catalytic process (*32*, *33*). Investigation over commercial Pt/C confirms a Tafel slope of 33 mV dec^{-1}, suggesting that the Tafel recombination step is the dominant process.

The electrocatalytic activities of the as-synthesized catalysts in an Ar-saturated alkaline medium (1.0 M KOH) are investigated. As shown in Fig. 5G, Pt@PCM also exhibits good electrocatalytic activity for HER, with a small overpotential of 139 mV at the current density of 10 mA cm^{-2} in this alkaline environment. The performance of Pt@PCM is better than that of Pt@PCM-0.095% and pure PCM with overpotentials of 281 and 471 mV, respectively. The Pt@PCM catalyst shows a Tafel slope of 73.6 mV dec^{-1} in the alkaline solution, which is lower than that of Pt@PCM-0.095% and pure PCM (Fig. 5H). These results further confirm that the decoration of platinum atoms into the lattice of PCM can lead to excellent electrocatalytic performance in both acidic and alkaline media (*34*).

The electrochemical stability of Pt@PCM in acidic and alkaline media is investigated by the current-time (*I-t*) test at a constant bias of −0.15 V versus RHE (Fig. 5I). Pt@PCM shows excellent stability, with less than 5% degradation of the initial current after 5 hours in both acidic and alkaline media. In addition, a slight fading of activity is observed after long-term potential cycling in the acidic environment, which further confirms the high corrosion resistance of the Pt@PCM (fig. S13). Recycled Pt@PCM after the *I-t* test is also characterized by TEM, Raman spectra, EXAFS, and platinum content analysis (figs. S14 to S17). No obvious change is observed, which indicates that the Pt@PCM is quite stable during the reaction process. The high stability of the hybrids should be attributed to the confinement effects of the carbon matrix and the strong coordination bonding between the isolated Pt sites and adjacent C/N atoms.

To interpret the nature of the isolated Pt atoms in the Pt@PCM electrocatalysts, we investigated the influence of thiocyanate ions (SCN^-) on the HER activity of the Pt@PCM catalysts. The metal catalytic sites are widely known to be deactivated by the SCN^- under acidic conditions (*33*, *35*). With the introduction of SCN^- with a concentration of 5 mM into the acidic electrolyte, the overpotential of the Pt@PCM catalyst at the current intensity of 15 mA cm^{-2} increases from 123 to 247 mV. Further increasing the concentration of SCN^- to 10 mM does not result in additional deactivation of Pt@PCM, indicating that nearly all isolated platinum sites have been blocked (fig. S18). This value is still much lower than that of pure PCM without Pt decoration. These experimental studies elucidate that decorated Pt sites are not the sole origin for the high HER activity of Pt@PCM.

DISCUSSION

To interpret the experimental results discussed above and provide deeper atomistic insight into the catalytic contribution from Pt decoration, first-principles theoretical calculations for a model interface in Pt-decorated graphene are performed. As indicated by the calculated density of states (DOS) results, the decoration of Pt species generates some new hybridized electronic states in Pt@PCM (Fig. 6A). The emergence of new electronic states could be attributed to the hybridization between Pt (4f and 5d orbitals) and the neighboring nonmetal atoms, which is consistent with EXAFS analysis results (*36*, *37*). The graphitic nature of graphene is also greatly modified because of the electron transfer from the lattice-confined Pt centers to the adjacent C/N atoms (*38*), as evidenced by the greatly modified state density of C and N atoms (fig. S19). The increased electronic states could result in the promoted hydrogen adsorption ability of C/N atoms and thereby the HER activity (*23*). Corresponding distribution of charge densities has also been investigated to verify this conclusion. As shown in Fig. 6B, a majority of the charge density originates from Pt atoms in Pt@PCM, indicating that the lattice-confined Pt atoms contribute favorably to charge density distribution and thus enhance the catalytic activity. In vast contrast, only Pt atoms adjacent to the graphene can contribute to the charge density distribution in Pt cluster–loaded graphene (figs. S20 and S21). We have also built models of totally exposed and carbon layer–covered active sites for the DFT calculations. The free energy of hydrogen adsorption (ΔG_{H^*}) is revealed to be rather high on the exposed site but relatively low on the carbon layer–covered site. Neither case is favorable for the hydrogen evolution in the catalytic

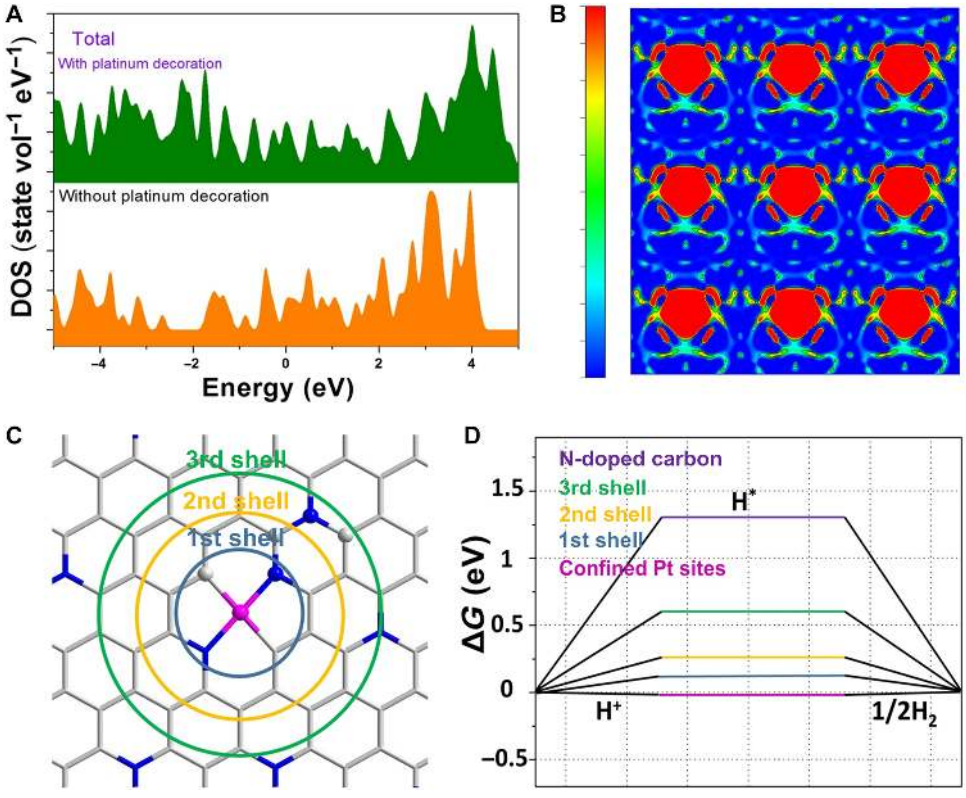

Fig. 6. DFT calculation results. (**A**) Calculated DOS of Pt@PCM and PCM. (**B**) Calculated distribution of charge density of Pt@PCM. (**C**) Schematic description for the coordination shells for the isolated Pt over the graphene. (**D**) ΔG_{H^*} on pure and Pt-decorated graphene in different coordination shells.

process (fig. S22). Our DFT results further confirm the advantage of confinement of isolated Pt atoms within the lattice of the carbon matrix.

To further clarify the enhanced activity with the decoration of Pt atoms, the ΔG_{H^*} of C and N atoms from Pt@PCM with different coordination shells is investigated (Fig. 6C) (*39*). The variations in the ΔG_{H^*} for the different coordination shells are used to describe the effect of the Pt confinement. As shown in Fig. 6D, the Pt confinement induces a change in ΔG_{H^*} of 1.05 eV in the first coordination shell, whereas the effect decreases with an increase in the number of shells. However, for the third coordination shell, the change still amounts to approximately 0.75 eV. These results demonstrate that the catalytic activity of inert graphene can be triggered via Pt decoration. Thus, confined Pt atoms and adjacent C and N atoms should be the active sites for HER.

In conclusion, a new model of single-atom decoration into the interior of the carbon matrix is proposed as an elegant platform to gain an atomic-level understanding of the electrocatalytic hydrogen evolution process. As a proof-of-concept prototype, our present study highlights the character of the PCM in providing specific structural and electronic environments for isolated Pt atoms. The isolated Pt centers maximize the atom utilization efficiency and exhibit significantly promoted catalytic activity. DFT investigation further confirms that the decoration of isolated Pt atoms can greatly modify the work function of the carbon matrix, resulting in the regulation of the ΔG_{H^*} that is close to zero. The heterogeneous catalysts with lattice-confined metal sites reported here provide crucial atomic-level insights and a new vision for the design of single-atom catalysts for other electrochemical processes, such as oxygen evolution, hydrogen oxidation, and CO_2 reduction.

MATERIALS AND METHODS

Preparation of PDA/PS-*b*-PEO

The precursor of PCM was prepared on the basis of a soft-templating synthetic strategy (*17*). In a typical synthesis, 200 mg of dopamine was dissolved in 12 ml of a mixed solution of ethanol and deionized water (with a volume ratio of 1:2). Then, the above mixture was poured into 4 ml of tetrahydrofuran containing 30 mg of diblock copolymer PS-*b*-PEO under mild stirring. After 1 hour, an ammonia aqueous solution was injected to induce the self-polymerization of dopamine. After continuous reaction for 20 hours, PDA/PS-*b*-PEO spheres were obtained by centrifugation and washing with the mixed solution of ethanol and deionized water for several times.

Preparation of Pt@PDA/PS-*b*-PEO

The as-prepared PDA/PS-*b*-PEO was first mixed with a certain amount of H_2PtCl_6 solution in a flask. Then, the flask was connected to the vacuum system and sonicated at 50°C for 4 hours, in which platinum components are located homogeneously on the surface of composite sphere with weak coordination.

Preparation of PCM and Pt@PCM

Carbonization of the PDA/PS-*b*-PEO composite at different temperature intervals (500°C for 2 hours and 800°C for 2 hours; heating rate, 1°C min^{-1}) was performed to remove the surfactants in the hybrid and produce PCM. A similar method was adopted to prepare the Pt-PCM, except that the sample of PDA/PS-*b*-PEO composite was replaced by Pt@PDA/PS-*b*-PEO.

Materials characterizations

TEM and HRTEM were conducted on a Tecnai G2 F30 S-Twin electron microscope operated at 300 kV. HAADF-STEM images and energy-dispersive x-ray (EDX) mappings were taken on a JEOL 2100F microscope. SEM images were recorded on a Hitachi S4800 microscope. Powder XRD was performed on an X'Pert PRO diffractometer with Cu Kα radiation (PANalytical). Small-angle x-ray scattering (SAXS) measurements (Rigaku NANO-Viewer) were used to evaluate the textural information on the nanoarchitectures. The SAXS instrument used a Cu Kα radiation (40 kV, 30 mA) source with a camera length of 700 mm. TG (Shimadzu DRG-60) was applied to trace the weight loss in the carbonization stage. Nitrogen adsorption-desorption isotherms were obtained by using a BELSORP-mini (MicrotracBEL Corp.) at 77 K. The surface areas were estimated by the multipoint Brunauer-Emmett-Teller method at a P/P_0 range of 0.05 to 0.5 based on the adsorption data. The total pore volumes and pore size distributions were calculated from the adsorption branches of isotherms based on the Barrett-Joyner-Halenda model. ICP-MS was performed on a Thermo IRIS Intrepid II XSP spectrometer. Before measuring, the samples were degassed in a vacuum at 120°C for 12 hours. Surface chemical analysis was performed by XPS (PHI Quantera SXM, ULVAC-PHI Inc.).

X-ray absorption data collection, analysis, and modeling

The Pt L_3-edge EXAFS and XANES spectra of as-prepared samples were acquired at 1W1B beamline of Beijing Synchrotron Radiation Facility, China in fluorescence mode using a Si(111) double-crystal monochromator under ambient conditions. The incident and fluorescence x-ray intensities were detected by a standard N_2-filled ionization chamber and a Lytle-type detector filled with Ar, respectively. The energy scale was calibrated using the spectrum of Pt foil (*40*). The EXAFS raw data were then background-subtracted, normalized, and Fourier-transformed by the standard procedures with the ATHENA program; least-squares curve fitting analysis of the EXAFS $\chi(k)$ data was carried out using the ARTEMIS program.

Electrochemical measurements

Electrochemical properties of the samples were characterized in a three-electrode cell with an electrochemical workstation (CH Instruments 650A). A carbon rod was used as the counter electrode, whereas an Ag/AgCl electrode was used as the reference electrode. LSV with a scan rate of 5 mV s^{-1} was carried out from 0.2 to −0.7 V versus RHE in electrolyte solution under continuous purging with Ar. The catalyst was cycled numerous times by CV until a stable CV curve was obtained before testing. For the preparation of the working electrode, 1.5 mg of as-synthesized catalyst was mixed with 20 μl of Nafion solution (5.0 wt % Nafion in ethanol) and 1000 μl of ethanol. The mixture was sonicated, and the suspension was pipetted out and dropped onto a glassy carbon electrode (GCE) with a diameter of 3 mm and then fully dried. All electrodes were prepared by depositing the same mass loading of catalysts on the GCE using an identical method. The onset potential refers to the potential where the current starts increasing from zero. The onset potentials were derived from the potentials corresponding to the current density of 0.2 mA cm^{-2}.

ECSA evaluation

The ECSA was estimated from the electrochemical double-layer capacitance of the hybrids. The electrochemical double-layer capacitance was determined from the CV curves measured in the

potential range of 0.42 to 0.62 V versus RHE according to the following equation

$$C_{dl} = I_c/\nu \quad (1)$$

where C_{dl}, I_c, and ν are the double-layer capacitance (in farads per square centimeter) of the electroactive materials, charging current (in milliamperes per square centimeter), and scan rate (in millivolts per second), respectively. I_c was taken at the potential of 0.52 V versus RHE.

TOF and mass activity calculation

The mass activity and TOF of the catalysts were calculated according to the following equations

$$\text{mass activity} = j/m \quad (2)$$

$$\text{TOF} = I/(2F \cdot n) \quad (3)$$

where j is the measured current density (in milliamperes per square centimeter), m is the catalyst loading (in milligrams per square centimeter), I is the current (in amperes), F is the Faraday constant (96,485.3 C mol^{-1}), and n is the number of moles of the active catalyst.

Computational methods

All calculations were performed using Vienna ab initio package based on the DFT. The generalized gradient approximation was used for the exchange-correlation energy. In addition, the D2 method proposed by Grimme was adopted to describe the van der Waals interactions (*49*). A plane-wave expansion for the basis set with a cutoff energy of 450 eV was used. A vacuum region of 20 Å was used to eliminate interactions between the neighboring cells of slab models. Monkhorst *k*-point meshes ($5 \times 5 \times 1$ and $2 \times 2 \times 1$) were used for the Brillouin-zone integrations of slab models with Pt doping and Pt cluster, respectively. All atoms were relaxed until the residual force was less than 0.01 eV/Å.

SUPPLEMENTARY MATERIALS

Supplementary material for this article is available at http://advances.sciencemag.org/cgi/content/full/4/1/eaao6657/DC1

fig. S1. SEM characterizations of PDA/PS-*b*-PEO.
fig. S2. Morphological and structural characterizations of Pt@PDA/PS-*b*-PEO.
fig. S3. TG and DSC analysis.
fig. S4. N 1s XPS spectra of Pt@PDA/PS-*b*-PEO after pyrolysis at different temperatures.
fig. S5. Pt 4f XPS spectra of Pt@PDA/PS-*b*-PEO after pyrolysis at different temperatures.
fig. S6. Wide-angle XRD analysis of the Pt species and their PCM supports.
fig. S7. EXAFS characterizations of Pt foil.
fig. S8. Elemental analysis of Pt/C-20%, PCM, and Pt@PCM.
fig. S9. Pore size distribution curves.
fig. S10. Low-angle XRD patterns.
fig. S11. Structural and compositional characterizations of the commercial Pt/C-20% catalyst.
fig. S12. CV curves at different scan rates for PCM.
fig. S13. Electrocatalytic durability of Pt@PCM.
fig. S14. TEM and HRTEM images of Pt@PCM after electrocatalysis.
fig. S15.Raman spectra of Pt@PCM before and after electrocatalysis.
fig. S16. XANES spectra of Pt@PCM before and after electrocatalysis.
fig. S17. EDX characterizations of Pt@PCM before and after electrocatalysis.
fig. S18. The influence of thiocyanate ions on the electrocatalytic performance of Pt@PCM.
fig. S19. DFT calculation results of Pt@PCM and PCM.
fig. S20. DFT calculation results of the platinum nanoparticle–loaded carbon matrix.
fig. S21. Constructed model for isolated platinum atoms.
fig. S22. DFT calculation results of exposed and carbon layer–covered platinum site.
table S1. Zeta potentials of PDA/PS-*b*-PEO and Pt@PDA/PS-*b*-PEO.
table S2. The ratios of different N species in Pt@PDA/PS-*b*-PEO after pyrolysis at different temperatures.
table S3. Fitting results of Pt L_3-edge EXAFS curves.
table S4. Physicochemical properties and elemental compositions of the samples.
table S5. Summary of representative HER catalysts in acidic electrolyte (0.5 M H_2SO_4).
References (*41*–*48*)

REFERENCES AND NOTES

1. J. Luo, J.-H. Im, M. T. Mayer, M. Schreier, M. K. Nazeeruddin, N.-G. Park, S. D. Tilley, H. J. Fan, M. Grätzel, Water photolysis at 12.3% efficiency via perovskite photovoltaics and earth-abundant catalysts. *Science* **345**, 1593–1596 (2014).
2. M. Cabán-Acevedo, M. L. Stone, J. Schmidt, J. G. Thomas, Q. Ding, H.-C. Chang, M.-L. Tsai, J.-H. He, S. Jin, Efficient hydrogen evolution catalysis using ternary pyrite-type cobalt phosphosulphide. *Nat. Mater.* **14**, 1245–1251 (2015).
3. J. A. Turner, Sustainable hydrogen production. *Science* **305**, 972–974 (2004).
4. M. S. Faber, S. Jin, Earth-abundant inorganic electrocatalysts and their nanostructures for energy conversion applications. *Energy Environ. Sci.* **7**, 3519–3542 (2014).
5. X.-F. Yang, A. Wang, B. Qiao, J. Li, J. Liu, T. Zhang, Single-atom catalysts: A new frontier in heterogeneous catalysis. *Acc. Chem. Res.* **46**, 1740–1748 (2013).
6. E. C. Tyo, S. Vajda, Catalysis by clusters with precise numbers of atoms. *Nat. Nanotechnol.* **10**, 577–588 (2015).
7. H. Zhang, G. Liu, L. Shi, J. Ye, Single-atom catalysts: Emerging multifunctional materials in heterogeneous catalysis. *Adv. Energy Mater.* **8**, 1701343 (2018).
8. H. Zhang, J. Wei, J. Dong, G. Liu, L. Shi, P. An, G. Zhao, J. Kong, X. Wang, X. Meng, J. Zhang, J. Ye, Efficient visible-light-driven carbon dioxide reduction by a single-atom implanted metal-organic framework. *Angew. Chem. Int. Ed.* **55**, 14310–14314 (2016).
9. B. Li, H.-M. Wen, Y. Cui, W. Zhou, G. Qian, B. Chen, Emerging multifunctional metal-organic framework materials. *Adv. Mater.* **28**, 8819–8860 (2016).
10. H. Yin, S. Zhao, K. Zhao, A. Muqsit, H. Tang, L. Chang, H. Zhao, Y. Gao, Z. Tang, Ultrathin platinum nanowires grown on single-layered nickel hydroxide with high hydrogen evolution activity. *Nat. Commun.* **6**, 6430 (2015).
11. F. R. Lucci, J. Liu, M. D. Marcinkowski, M. Yang, L. F. Allard, M. Flytzani-Stephanopoulos, E. C. H. Sykes, Selective hydrogenation of 1,3-butadiene on platinum-copper alloys at the single-atom limit. *Nat. Commun.* **6**, 8550 (2015).
12. L. Lin, W. Zhou, R. Gao, S. Yao, X. Zhang, W. Xu, S. Zheng, Z. Jiang, Q. Yu, Y.-W. Li, C. Shi, X.-D. Wen, D. Ma, Low-temperature hydrogen production from water and methanol using Pt/α-MoC catalysts. *Nature* **544**, 80–83 (2017).
13. Y. Zheng, Y. Jiao, Y. Zhu, L. H. Li, Y. Han, Y. Chen, M. Jaroniec, S.-Z. Qiao, High electrocatalytic hydrogen evolution activity of an anomalous ruthenium catalyst. *J. Am. Chem. Soc.* **138**, 16174–16181 (2016).
14. Y. Zheng, Y. Jiao, Y. Zhu, Q. Cai, A. Vasileff, L. H. Li, Y. Han, Y. Chen, S.-Z. Qiao, Molecule-level *g*-C_3N_4 coordinated transition metals as a new class of electrocatalysts for oxygen electrode reactions. *J. Am. Chem. Soc.* **139**, 3336–3339 (2017).
15. P. Liu, Y. Zhao, R. Qin, S. Mo, G. Chen, L. Gu, D. M. Chevrier, P. Zhang, Q. Guo, D. Zang, B Wu, G Fu, N Zheng, Photochemical route for synthesizing atomically dispersed palladium catalysts. *Science* **352**, 797–800 (2016).
16. B. Bayatsarmadi, Y. Zheng, A. Vasileff, S.-Z. Qiao, Recent advances in atomic metal doping of carbon-based nanomaterials for energy conversion. *Small* **13**, 1700191 (2017).
17. J. Tang, J. Liu, C. Li, Y. Li, M. O. Tade, S. Dai, Y. Yamauchi, Synthesis of nitrogen-doped mesoporous carbon spheres with extra-large pores through assembly of diblock copolymer micelles. *Angew. Chem. Int. Ed.* **54**, 588–593 (2015).
18. T. Yang, H. Ling, J.-F. Lamonier, M. Jaroniec, J. Huang, M. J. Monteiro, J. Liu, A synthetic strategy for carbon nanospheres impregnated with highly monodispersed metal nanoparticles. *NPG Asia Mater.* **8**, e240 (2016).
19. H. Funke, A. Scheinost, M. Chukalina, Wavelet analysis of extended x-ray absorption fine structure data. *Phys. Rev. B* **71**, 094110 (2005).
20. H. Fei, J. Dong, M. J. Arellano-Jiménez, G. Ye, N. D. Kim, E. L. G. Samuel, Z. Peng, Z. Zhu, F. Qin, J. Bao, Atomic cobalt on nitrogen-doped graphene for hydrogen generation. *Nat. Commun.* **6**, 8868 (2015).
21. P. Hu, Z. Huang, Z. Amghouz, M. Makkee, F. Xu, F. Kapteijn, A. Dikhtiarenko, Y. Chen, X. Gu, X. Tang, Electronic metal–support interactions in single-atom catalysts. *Angew. Chem. Int. Ed.* **53**, 3418–3421 (2014).
22. J. Tang, R. R. Salunkhe, J. Liu, N. L. Torad, M. Imura, S. Furukawa, Y. Yamauchi, Thermal conversion of core–shell metal–organic frameworks: A new method for selectively functionalized nanoporous hybrid carbon. *J. Am. Chem. Soc.* **137**, 1572–1580 (2015).
23. K. Kamiya, R. Kamai, K. Hashimoto, S. Nakanishi, Platinum-modified covalent triazine frameworks hybridized with carbon nanoparticles as methanol-tolerant oxygen reduction electrocatalysts. *Nat. Commun.* **5**, 5040 (2014).
24. D. J. Martin, K. Qiu, S. A. Shevlin, A. D. Handoko, X. Chen, Z. Guo, J. Tang, Highly efficient photocatalytic H_2 evolution from water using visible light and structure-controlled graphitic carbon nitride. *Angew. Chem. Int. Ed.* **53**, 9240–9245 (2014).

25. R. Liu, P. Wang, X. Wang, H. Yu, J. Yu, UV-and visible-light photocatalytic activity of simultaneously deposited and doped Ag/Ag(I)-TiO_2 photocatalyst. *J. Phys. Chem. C* **116**, 17721–17728 (2012).
26. H. Zhang, Z. Ma, G. Liu, L. Shi, J. Tang, H. Pang, K. Wu, T. Takei, J. Zhang, Y. Yamauchi, J. Ye, Highly active nonprecious metal hydrogen evolution electrocatalyst: Ultrafine molybdenum carbide nanoparticles embedded into a 3D nitrogen-implanted carbon matrix. *NPG Asia Mater.* **8**, e293 (2016).
27. B. Jiang, C. Li, Ö. Dag, H. Abe, T. Takei, T. Imai, M. S. A. Hossain, M. T. Islam, K. Wood, J. Henzie, Y. Yamauchi, Mesoporous metallic rhodium nanoparticles. *Nat. Commun.* **8**, 15581 (2017).
28. H. Zhang, Z. Ma, J. Duan, H. Liu, G. Liu, T. Wang, K. Chang, M. Li, L. Shi, X. Meng, K Wu, J Ye, Active sites implanted carbon cages in core–shell architecture: Highly active and durable electrocatalyst for hydrogen evolution reaction. *ACS Nano* **10**, 684–694 (2015).
29. Y. Jiao, Y. Zheng, K. Davey, S.-Z. Qiao, Activity origin and catalyst design principles for electrocatalytic hydrogen evolution on heteroatom-doped graphene. *Nat. Energy* **1**, 16130 (2016).
30. A. B. Laursen, K. R. Patraju, M. J. Whitaker, M. Retuerto, T. Sarkar, N. Yao, K. V. Ramanujachary, M. Greenblatt, G. C. Dismukes, Nanocrystalline Ni_5P_4: A hydrogen evolution electrocatalyst of exceptional efficiency in both alkaline and acidic media. *Energy Environ. Sci.* **8**, 1027–1034 (2015).
31. J. R. McKone, B. F. Sadtler, C. A. Werlang, N. S. Lewis, H. B. Gray, Ni–Mo nanopowders for efficient electrochemical hydrogen evolution. *ACS Catal.* **3**, 166–169 (2013).
32. D. Y. Chung, S. W. Jun, G. Yoon, H. Kim, J. M. Yoo, K.-S. Lee, T. Kim, H. Shin, A. K. Sinha, S. G. Kwon, Large-scale synthesis of carbon-shell-coated FeP nanoparticles for robust hydrogen evolution reaction electrocatalyst. *J. Am. Chem. Soc.* **139**, 6669–6674 (2017).
33. A. Mazumdar, D. Bandyopadhyay, U. Bandyopadhyay, R. K. Banerjee, Probing the role of active site histidine residues in the catalytic activity of lacrimal gland peroxidase. *Mol. Cell. Biochem.* **237**, 21–30 (2002).
34. H. Zhang, J. Nai, L. Yu, X. W. Lou, Metal-organic-framework-based materials as platforms for renewable energy and environmental applications. *Joule* **1**, 77–107 (2017).
35. C. H. Londergan, R. Baskin, C. G. Bischak, K. W. Hoffman, D. M. Snead, C. Reynoso, Dynamic asymmetry and the role of the conserved active-site thiol in rabbit muscle creatine kinase. *Biochemistry* **54**, 83–95 (2015).
36. B. Qiao, A. Wang, X. Yang, L. F. Allard, Z. Jiang, Y. Cui, J. Liu, J. Li, T. Zhang, Single-atom catalysis of CO oxidation using Pt_1/FeO_x. *Nat. Chem.* **3**, 634–641 (2011).
37. J. Deng, H. Li, J. Xiao, Y. Tu, D. Deng, H. Yang, H. Tian, J. Li, P. Ren, X. Bao, Triggering the electrocatalytic hydrogen evolution activity of the inert two-dimensional MoS_2 surface via single-atom metal doping. *Energy Environ. Sci.* **8**, 1594–1601 (2015).
38. H. Zhang, T. Wang, J. Wang, H. Liu, T. D. Dao, M. Li, G. Liu, X. Meng, K. Chang, L. Shi, T. Nagao, J. Ye, Surface plasmon enhanced photodriven CO_2 reduction catalyzed by metal organic framework derived iron nanoparticles encapsulated by ultrathin carbon layers. *Adv. Mater.* **28**, 3703–3710 (2016).
39. J. Greeley, T. F. Jaramillo, J. Bonde, I. Chorkendorff, J. K. Nørskov, Computational high-throughput screening of electrocatalytic materials for hydrogen evolution. *Nat. Mater.* **5**, 909–913 (2006).
40. B. Ravel, M. Newville, *ATHENA, ARTEMIS, HEPHAESTUS*: Data analysis for X-ray absorption spectroscopy using IFEFFIT. *J. Synchrotron Radiat.* **12**, 537–541 (2005).
41. J. Kibsgaard, T. F. Jaramillo, F. Besenbacher, Building an appropriate active-site motif into a hydrogen-evolution catalyst with thiomolybdate $[Mo_3S_{13}]^{2-}$ clusters. *Nat. Chem.* **6**, 248–253 (2014).
42. J. Deng, H. Li, S. Wang, D. Ding, M. Chen, C. Liu, Z. Tian, K. S. Novoselov, C. Ma, D. Deng, X. Bao, Multiscale structural and electronic control of molybdenum disulfide foam for highly efficient hydrogen production. *Nat. Commun.* **8**, 14430 (2017).
43. D. Voiry, H. Yamaguchi, J. Li, R. Silva, D. C. B. Alves, T. Fujita, M. Chen, T. Asefa, V. B. Shenoy, G. Eda, M. Chhowalla, Enhanced catalytic activity in strained chemically exfoliated WS_2 nanosheets for hydrogen evolution. *Nat. Mater.* **12**, 850–855 (2013).
44. J. Deng, P. Ren, D. Deng, L. Yu, F. Yang, X. Bao, Highly active and durable non-precious-metal catalysts encapsulated in carbon nanotubes for hydrogen evolution reaction. *Energy Environ. Sci.* **7**, 1919–1923 (2014).
45. P. Xiao, M. A. Sk, L. Thia, X. Ge, R. J. Lim, J.-Y. Wang, K. H. Lim, X. Wang, Molybdenum phosphide as an efficient electrocatalyst for the hydrogen evolution reaction. *Energy Environ. Sci.* **7**, 2624–2629 (2014).
46. X. Zou, X. Huang, A. Goswami, R. Silva, B. R. Sathe, E. Mikmeková, T. Asefa, Cobalt-embedded nitrogen-rich carbon nanotubes efficiently catalyze hydrogen evolution reaction at all pH values. *Angew. Chem. Int. Ed.* **53**, 4372–4376 (2014).
47. Y. Hou, Z. Wen, S. Cui, S. Ci, S. Mao, J. Chen, An advanced nitrogen-doped graphene/cobalt-embedded porous carbon polyhedron hybrid for efficient catalysis of oxygen reduction and water splitting. *Adv. Funct. Mater.* **25**, 872–882 (2015).
48. Y. Zheng, Y. Jiao, L. Zhu, H. Li, Y. Han, Y. Chen, A. Du, M. Jaroniec, S. Z. Qiao, Hydrogen evolution by a metal-free electrocatalyst. *Nat. Commun.* **5**, 3783 (2014).
49. S. Grrime, Semiempirical GGA-type density functional constructed with a long-range dispersion correction. *J. Comput. Chem.* **27**, 1787–1799 (2016).

Acknowledgments

Funding: X.W.L. acknowledges the funding support from the National Research Foundation (NRF) of Singapore via the NRF Investigatorship (NRF-NRFI2016-04). **Author contributions:** H.Z. and X.W.L. conceived the idea. H.Z. carried out the materials synthesis. H.Z., P.A., B.Y.G., and J.D. carried out materials characterizations and electrochemical measurements. W.Z. performed the DFT calculations. H.Z., P.Z., and X.W.L. discussed the results and co-wrote the manuscript. All authors read and commented on the manuscript. **Competing interests:** The authors declare that they have no competing interests. **Data and materials availability:** All data needed to evaluate the conclusions in the paper are present in the paper and/or the Supplementary Materials. Additional data related to this paper may be requested from the authors.

Submitted 14 August 2017
Accepted 11 December 2017
Published 19 January 2018
10.1126/sciadv.aao6657

Citation: H. Zhang, P. An, W. Zhou, B. Y. Guan, P. Zhang, J. Dong, X. W. Lou, Dynamic traction of lattice-confined platinum atoms into mesoporous carbon matrix for hydrogen evolution reaction. *Sci. Adv.* **4**, eaao6657 (2018).